Confinement Induced Oscillation of a cylinder at Reynolds number below the Vortex Induced Vibration Flow-induced oscillation of a confined tethered cylinder below the vortex shedding threshold

Benoît Semin, Astrid Decoene, Jean-Pierre Hulin, Marc L.M. François, Harold Auradou

Confinement Induced Oscillation of a cylinder at Reynolds number below the Vortex Induced Vibration Flow-induced oscillation of a confined tethered cylinder below the vortex shedding threshold

By B. SEMIN[1], A. DECOENE[2], J.-P. HULIN[1] M.L.M. FRANÇOIS[1] AND H. AURADOU[1]

[1]Univ. Pierre et Marie Curie-Paris 6, Univ. Paris-Sud, CNRS, F-91405. Lab. FAST, Bat. 502, Campus Univ., Orsay, F-91405, France.

[2]Department of mathematics, Univ. Paris-Sud, Bat. 452, Campus Univ., Orsay, F-91405, France.

(Received ?? and in revised form ??)

A new type of flow induced oscillation has been observed by placing a tethered cylinder in a Hele Shaw cell. This novel instability is studied numerically and experimentally as function of the Reynolds number and as function of the mass of the cylinder in Hele Shaw cell such that the cylinder diameter to cell aperture ratio: $D = 0.66$). The cylinder is found to oscillates above a Reynolds number $Re_c \simeq 20$. This critical Re is much lower than the threshold for Bénard–Von Kármán vortex shedding behind a fixed cylinder in the same configuration. Close to the threshold, the growth rate of the amplitude varies like $(Re - Re_c)^{1/2}$ and the lack of hysteresis demonstrate that the process is a supercritical Hopf bifurcation. The adjustement of the position of the cylinder by a Van der Pol equation allows for the identification of the stiffness, the amplification coefficient and to study the effect of the total mass: Forced oscillation is used to study their behavior and their physical meaning is discussed using the pressure field. For dense cylinder, the CIV is observed to end abruptly and new oscillations are observed when the Re is increased above 110; this oscillation corresponds to Vortex Induced Vibration (VIV). If the mass falls below a critical value, the CIV is not observed to vanish.

Flow–structure coupling, oscillatory instability

1. Introduction

Flow induced oscillations of slender structures facing a flow are of interest in many domains of engineering such as the design of tubular structures of offshore platforms, heat exchangers or chemical reactors (see for instance **??**). Most previous experimental and numerical fundamental studies often considered a rigid circular cylinder transverse to a fluid flow with no lateral confinement and with only one degree of freedom perpendicular to both the flow and to the axis of the cylinder (see for instance **???**).

The present work deals, in contrast, with a tethered cylinder strongly confined between two parallel plane walls: the confinement, characterised by the ratio between the cylinder diameter $\bar{D}$ and the cell aperture $\bar{h}$, is equal to 0.66. This configuration corresponds to important recent applications at lower Reynolds numbers such as the enhancement of

mixing or heat exchange in microfluidic circuits (see **?**) or the design of energy-harvesting devices on a chip (**?**). Our experiments show that, when sufficiently confined, a cylinder oscillates spontaneously when $Re \simeq 20$ (where the Reynolds number Re is defined using the mean velocity and the aperture $\bar{h}$). This is well below the threshold for Bénard–Von Kármán vortex shedding (111 for this particular geometry).

This implies that the instability mechanism in the present experiments differs from that of vortex induced vibrations reported in early studies. The latter considered dense cylinders constrained elastically: their transverse position satisfies a forced damped harmonic oscillator equation in which the driving force term is associated to the fluctuating lift induced by vortex shedding.

Recent studies investigated related effects either at Reynolds numbers below the vortex shedding threshold or for structures without a natural frequency. In the first case, oscillations have been predicted numerically by **?** and **?**, but only if an external elastic restoring force was present. In the second, **?** considered a massless cylinder with no restoring force: however, the Reynolds number was higher than here (100) so that vortex shedding took place. Still at high Reynolds numbers and with no restoring force, experiments by **?** demonstrated that large amplitude vibrations occur below a critical value of the mass; the same observation was made on transverse motions of the trajectory of light cylinders rising in a stationary fluid by **?**.

The effect of a weak confinement has been studied numerically by **?** in the case where the fluid is allowed to slip at the walls, and by **?** in the no-slip case. In the latter study, a slight amplitude decrease and a large frequency variation was observed. In a recent work, **?** investigated numerically the effect of the confinement by studying the displacement of a square cylinder strongly confined between two parallel walls (ratio between the side of the cylinder and the distance between walls equal to 0.4). Regular oscillations are observed for cylinders dense enough and are accounted for by vortex shedding; below a critical mass, there is a second regime in which the motion is highly irregular with a near continuum spectrum. No quantitative interpretation of these results was however attempted.

The present study is focused on a thorough description and modelling of the instability of a tethered circular cylinder in a strongly confined Hele-Shaw cell geometry and at Reynolds numbers below the vortex shedding threshold. The experimental setup is described in § 2 and the numerical procedure in § 3. The characteristics of the oscillations, in both the permanent and transient regimes, are discussed in § 4. A dynamical system approach is then used in § 5 to analyse these results: we found that the properties of the system are well described quantitatively by the non linear Van der Pol equation. In § 6 these results are compared quantitatively to the free oscillations in the permanent and transient regimes and the influence of the control parameters on the instability threshold is investigated. Finally, § 7 is devoted to the physical interpretation of the coefficients of the Van der Pol model: the coexistence of viscous and inertial effects is found to be a key element leading to this hydrodynamic instability.

2. Experimental setup

The experimental setup is shown in figure 1: it consists of a Hele-Saw cell made of two transparent parallel Plexiglas plates, inside which a fluid flows vertically downwards. The lateral sides of the cell are also transparent allowing for the visualisation in the gap of the cell. It has a constant aperture $\bar{h} = 4.9 \pm 0.1$ mm and width $\bar{W} = 90 \pm 0.1$ mm. Note that, in this article, dimensional variables are displayed with an overbar ($\bar{W}$, $\bar{h}$,...) in contrast with dimensionless ones.

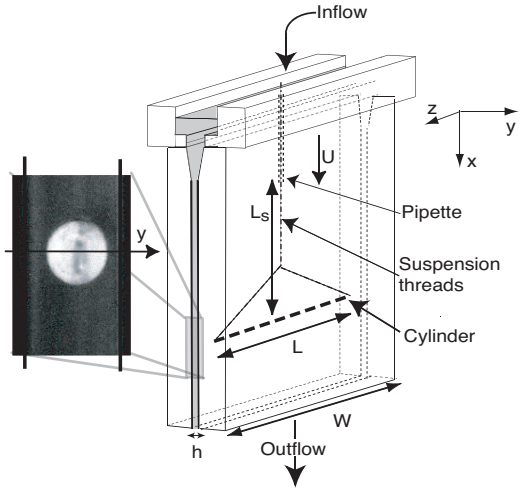

FIGURE 1. Schematic view of the experimental setup.

A Plexiglas cylinder of diameter $\bar{D} = 3.2 \pm 0.1$ mm is placed horizontally in the gap. Its density $\bar{\rho}_s = 1190\,\mathrm{kg\,m^{-3}}$ is close to that of water in order to reduce buoyancy effects (see § 4 for a detailed discussion of the gravity effects). In order to minimise the bypass flow at the ends of the cylinder, its length $\bar{L}$ is almost equal to the width of the cell ($\bar{L}/\bar{W} > 0.98$) (see **?**). The ends of the cylinder are attached by nylon threads of diameter 0.1 mm to a fixed suspension point located close to the inlet (see figure 1). The distance between this point and the cylinder is $\bar{L}_s = 150$ mm, i.e. much larger than the aperture $\bar{h}$ of the cell. In this way, the cylinder can only move in the direction y normal to the cell walls (but the displacement can vary along z).

The motion of the cylinder in the aperture of the Hele-Shaw cell is analysed by a Pixelink computer controlled video camera at a constant frame rate of 22 fps (the resolution is 20 pixels per mm). The displacement of the centre of the cylinder is determined using the method of virtual image correlation (see **?**). A virtual image of a disc is first created, with a radius larger than the one of the cylinder in the experimental image and with a grey level varying continuously from 1 (maximal value) at the centre to 0 at its border. The location of the centre of the cylinder is then assumed to correspond to that of the virtual disc when the correlation between the experimental image and the virtual image is optimal. In some experiments, a second video camera was placed on the other lateral side of the cell to verify that the axis of the cylinder remains parallel to the z axis. The absence of rotation around the cylinder axis z has also been verified by observing the motion of defects of the cylinder surface.

The fluid is sucked at the bottom of the cell at a constant flow rate by a gear pump (Ismatec MCP-Z) and is then reinjected into the open bath at the top. The mean flow is perpendicular to the axis of the cylinder (x direction) and the maximal flow rate is $500\,\mathrm{mL\,min^{-1}}$. Two fluids are used: water and an aqueous solution containing $1\,\mathrm{g\,L^{-1}}$ of natrosol. The fluids have the same density but different viscosities. The viscosity of water was estimated using a temperature measurement and tabulated values (see **?**), and is equal to $\bar{\mu} = 0.88 \pm 0.05$ mPa s. A Contraves low shear 30 viscosimeter was used to measure the viscosity and to check the Newtonian nature of the natrosol solution. In the range of shear rates accessible by the rheometer, i.e. 1 to $100\,\mathrm{s^{-1}}$, the viscosity was found to be constant and equal to $\bar{\mu} = 1.28 \pm 0.05$ mPa s. In order to increase the

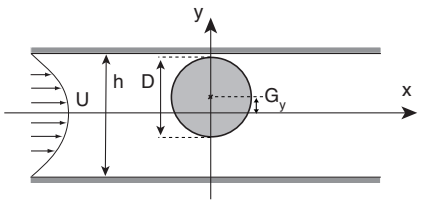

FIGURE 2. Schematic two-dimensional representation of the numerical configuration.

optical contrast between the fluids and the transparent cylinder, a small amount of dye (nigrosin, 0.1 $\mathrm{g\,L^{-1}}$) is added to the fluids.

3. Numerical procedure

The velocity and pressure fields as well as the forces on the cylinder were computed by two-dimensional numerical simulations. A schematic view of the numerical configuration is shown on figure 2.

The fluid is modelled using the incompressible Navier–Stokes equations with no-slip boundary conditions on the walls and on the surface of the cylinder. A Poiseuille parabolic velocity profile, constant in time, is imposed at the inlet and a stress-free condition at the outlet. Like in the experiment, the motion of the cylinder is restricted to the y direction. The cylinder is a rigid body and is not allowed to rotate. The motion of the cylinder is given by the component along y of Newton's second law (along x, the hydrodynamic force is balanced by the tension of the thread).

These equations are solved in a strongly coupled way, using a method similar to the one developed by **?** and **?**. In order to take suitably into account the fluid–cylinder coupling, a single variational form is written on the whole domain, including both the fluid and the cylinder. The constraint due to the rigid motion of the cylinder is handled by penalty, and that due to the suspension threads by duality (the Lagrange multiplier corresponds to the thread tension). In order to deal with the moving rigid domain, the problem is written in an Arbitrary Lagrangian-Eulerian formulation (see **?**). The advection term is treated using a method of characteristics (see **?**), and the variational problem obtained is solved by means of the finite element solver FreeFem++ (see **?**).

The aperture $\bar{h}$, the mean velocity of the fluid $\bar{U}$ and the density of the fluid $\bar{\rho}_f$ are used to define the Reynolds number $Re = \bar{\rho}_f \bar{U} \bar{h}/\bar{\mu}$ and to make the equation and the results dimensionless: the dimensionless diameter D is, for instance, equal to the ratio $\bar{D}/\bar{h}$, and the dimensionless cylinder density ρ_s is the ratio of the density of the cylinder by the density of the fluid. The dimensionless frequency f is defined by $f = \bar{f}\bar{h}/\bar{U}$ and is equal to the Strouhal number of the phenomenon when $\bar{h}$ is used as the characteristic length.

The size of the domain in the direction of the flow ranges from $x = -5h$ to $x = 7h$ and it contains more than 6 000 nodes. In order to accurately describe the shape of the cylinder and its evolution in time, the mesh exactly follows the motion of the cylinder along the $y-$direction. Inside the fluid domain, the mesh is subjected to a displacement which satisfies the right boundary conditions and ensures the non-degeneration of mesh cells.

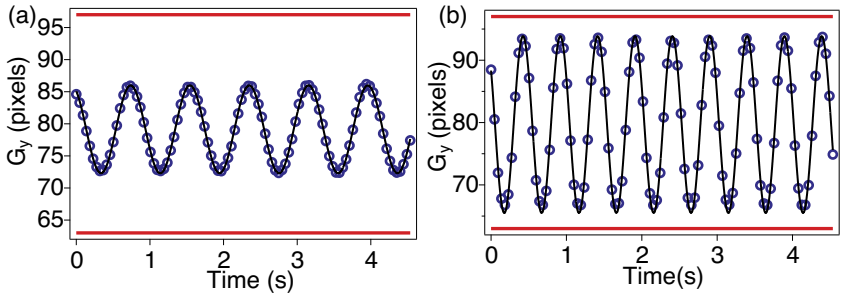

FIGURE 3. Experimental variation of the transverse co-ordinate $\bar{y}$ of the centre of the cylinder as a function of time for two different Re. (a): $Re = 25$, (b): $Re = 50$. Continuous line: fit of the experimental variation by a sine wave. Horizontal dotted lines: maximum possible amplitude of the oscillation (cylinder getting in contact with the walls).

4. Observation and characterisation of the instability

Experimentally, when the flow rate is progressively increased from zero, the cylinder moves towards a stable position half way between the walls. Then, for a Reynolds number Re above 20, it starts to oscillate spontaneously in the y direction with its axis remaining parallel to z. Figure 3 displays the experimental variation with time of the location $\bar{y}$ of the axis of the cylinder. The oscillation is regular and stable, and well fitted by the sine function:

$$y(t) = A\sin(2\pi f t + \varphi), \tag{4.1}$$

where A and f are the amplitude and frequency of the oscillation (the phase φ takes any value depending on the time origin). Even for Re well above 20 (see figure 3b), the oscillation is still accurately fitted by a sine wave. The same fit is also valid for the numerical results.

We tested experimentally the effect of of the gravity and of the drag component along y by reducing the length to $\bar{L}_s = 65$ mm. The frequency at $Re = 20$ changes by less than 5%, and the amplitude by less than 10% (the discrepancies decrease with Re). We also performed numerical simulation where both the gravity (along x) and the finite length ($\bar{L}_s = 150$ mm) of the threads are taken into account. At $Re = 20$, the frequency increase and the amplitude decrease compared to the simulations without gravity and with an infinite thread length are less than 6% (the discrepancies also decrease with Re). This confirm that gravity and the drag on the cylinder have only a small influence in our experiments.

Figure 4 displays the variations of the dimensionless amplitude and frequency (or Strouhal number) of the oscillations as a function of Re. Using this normalisation, the experimental measurements performed with the two fluids collapse onto a single curve, which is confirm that the normalisation is relevant. The numerical threshold and frequency (solid lines in Fig. 4) also agree within 25% with the experimental measurements without requiring any adjustable parameter. This difference may be partly accounted for the three-dimensional effects: the shearing of the thin fluid layer between the lateral wall and the end of the cylinder results in a viscous force on the latter. Drag forces (along y) on the suspension threads may also influence the dynamics of the cylinder. Gravity and drag on the cylinder can only explain a small part of this discrepancy, as discussed in the previous paragraph.

The amplitude of the oscillations increases steeply with Re above the threshold and then tends towards a constant value reflecting its limitation by the walls, for the density of

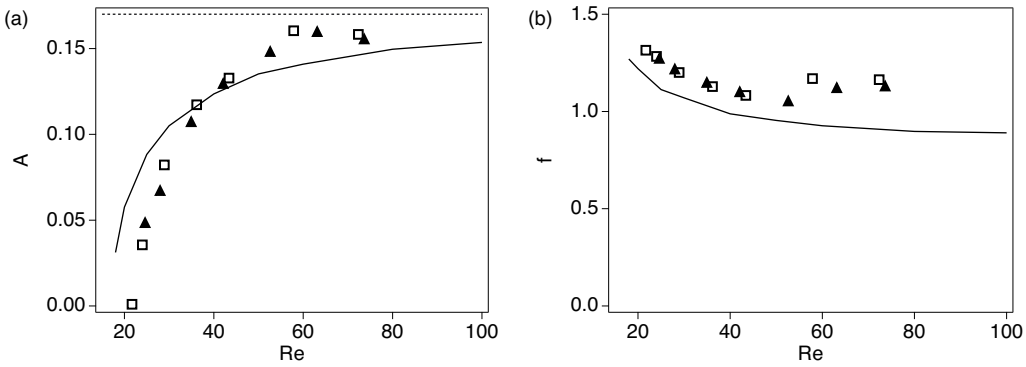

FIGURE 4. Dimensionless amplitude A and frequency f measured experimentally and numerically at $\rho_s = 1.19$. ○: experiments using water, □: experiments using an aqueous natrosol solution, solid line: numerical results. Dotted line: maximal possible amplitude of the oscillation.

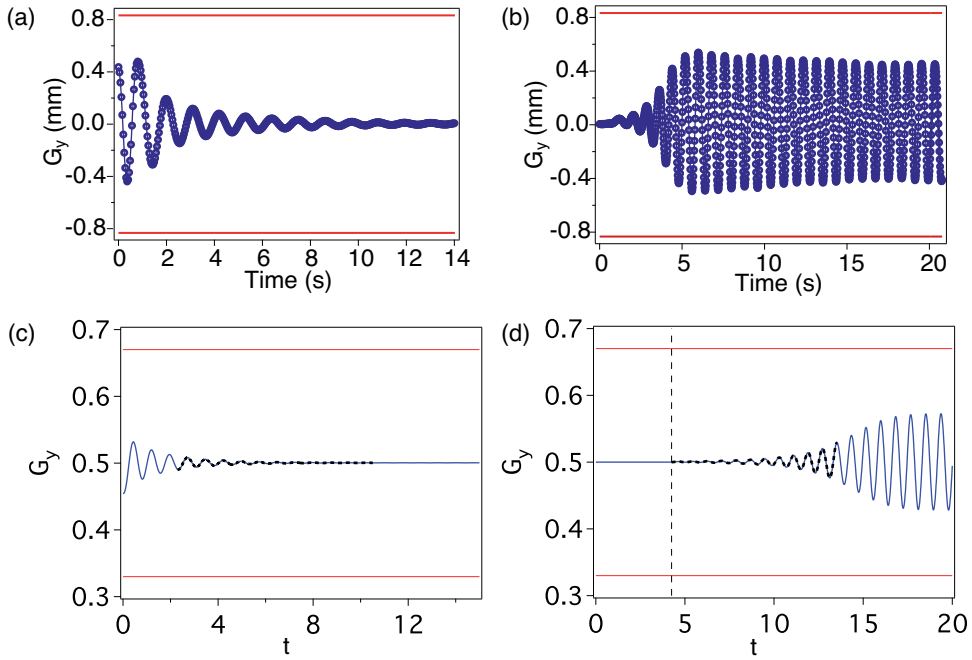

FIGURE 5. Time variation of the displacement y in the transient regime. Experiments: (a) Re is reduced from 27 to 17 at $t = 0$; (b): Re is increased from 17 to 27 at $t = 0$. Numerical simulations: (c) $Re = 14$, (d) $Re = 22$. Horizontal dotted lines: maximal possible amplitude. Grey dotted lines in (c) and (d): fit with (4.2)

the cylinder $\rho_s = 1.19$ corresponding to the experiments (for other density, see figure 12). The Strouhal number decreases weakly with Re which corresponds to a nearly linear increase of the dimensional frequency $\bar{f}$ with the mean flow velocity (or equivalently with the flow rate).

The dynamics of the instability has been investigated by decreasing or increasing stepwise the flow rate (and therefore Re) and studying the subsequent transient regime (see figures 5a and b). Equivalent information is obtained from the numerical simulations by

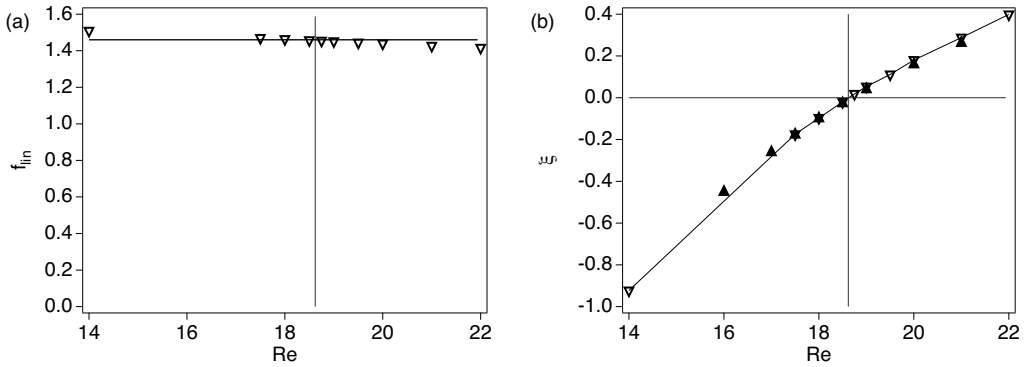

FIGURE 6. Variation as a function of Re of the frequency of the transient regime f_l and growth rate ξ of the free oscillations as obtained from numerical simulations; ∇: direct simulation of free oscillations; $\blacktriangle$: values deduced from the characteristics of forced oscillations; vertical dashed line: resonance frequency. Density of the cylinder $\rho_s = 0.01$.

assuming that the cylinder is released from an off-centre position at a Reynolds number $Re < Re_c$ (see figure 5c) or in the mid-plane of the cell for $Re > Re_c$ (see figure 5d).

Below Re_c, damped oscillations of the cylinder are observed and it finally comes to rest half way between the walls. At a Reynolds number larger than Re_c, the cylinder oscillates spontaneously with an amplitude increasing initially with time before reaching a constant value. In the experiments, there is, in addition, a small (still unexplained) overshoot at the end of the initial phase (see figure 5b).

When the amplitude is small (i.e. less than 10% of the aperture), the variation of y during the initial phase can be fitted by:

$$y(t) = A_0 \sin(2\pi f_l t + \varphi) \exp(\xi t), \tag{4.2}$$

in which f_l and ξ are respectively the frequency in the linear regime and the growth rate. The coefficients A_0 and φ depend on the choice of the time origin and have no physical meaning. The variation of the parameters f_l and ξ as a function of the Reynolds number have been obtained from the numerical simulations described above and are shown in figure 6 (∇ symbols). The frequency f_l is almost independent of Re while the growth rate increases monotonously with Re from negative to positive values. These different features show that, close to Re_c, the system can be considered as a weakly non linear oscillator with a well defined instability threshold.

The most common mechanism accounting for such flow induced oscillations in open geometries is the Bénard–Von Kármán vortex shedding instability. The possibility of its occurrence has been tested in the present case by keeping the cylinder at a fixed position and visualising the flow by means of a fluorescent dye (eosin) injected in a half section; a laser sheet perpendicular to the cylinder axis illuminates the downstream part of the flow. In these latter experiments, flow oscillations occur only above a threshold Reynolds number $Re_{\mathrm{BVK}} = 120 \pm 10$. Numerically, the corresponding threshold is equal to 111, which is similar to the value $Re_{\mathrm{BVK}} = 116$ inferred from the interpolation of the numerical data obtained by **?**. The confinement increases therefore significantly the threshold of the Bénard–Von Kármán instability compared to its value in open flows ($Re_{\mathrm{BVK}} = 47$). This confirms previous results by, for instance, **???**. To conclude, Re_{BVK} is much larger than the threshold values $Re_c \simeq 20$ measured here, so that a mechanism involving vortex shedding is unlikely; in § 7 we will confirm that the instability is not due to vortex shedding.

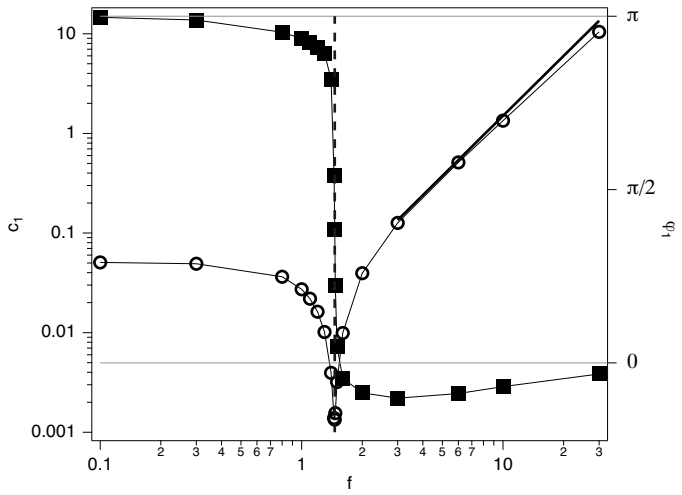

FIGURE 7. Variation of the amplitude F_1 (•) and phase ϕ_1 (■) of the lift force F_y as a function of the frequency f obtained from numerical simulations of the forced oscillations of the cylinder. Slope of thick straight line: 2. The dashed lines are guides for the eyes (vertical: values 0 and π of the phase, vertical: resonance frequency). Amplitude of forced oscillations: $A = 5 \times 10^{-4}$, $Re = 20$.

5. Dynamical system approach in forced oscillations regime.

In this §, we use a dynamical system approach to account for these observations. More precisely, we establish a differential equation satisfied by y and depending on a small number of parameters: these are determined by the results of numerical simulations of forced oscillations at different frequencies. This technique has been widely used both experimentally (see for example **??**) and numerically (see for example **??**). Practically, the displacement of the centre of the cylinder is forced to vary sinusoidally with time ($y(t) = A\sin(2\pi ft)$) and the simulations allow one to compute the total hydrodynamic lift force $F_y(t)$ on the cylinder. All numerical simulations are performed at a same Reynolds number $Re = 20$ (slightly above the numerical value of Re_c).

5.1. *Force response to a small amplitude excitation*

We first study the case in which the amplitude A is small enough (5×10^{-4}) to remain in the linear regime. In this case, the lift force F_y varies also sinusoidally with:

$$F_y = F_1 \sin(2\pi ft + \phi_1). \tag{5.1}$$

The phase ϕ_1 is chosen such that $F_1 \geqslant 0$. The variations of the amplitude F_1 and of the phase ϕ_1 of the force F_y as a function of the frequency f are displayed in figure 7.

In the low frequency limit, the instantaneous lift force F_y tends toward that of a fixed cylinder at the same location. The limiting value $\phi_1 = \pi$ of the phase (see right part of figure 7) implies that, for small amplitudes A, F_y is in a direction opposite to the displacement and proportional to it. In this case, the relation between F_y and y may be written:

$$F_y = -ky. \tag{5.2}$$

The parameter k represents the effective stiffness of the system and its value deduced from the numerical simulations is equal to 95. Figure 8 displays the variation of F_y with y obtained from a set of simulations for a fixed cylinder: it confirms the above results

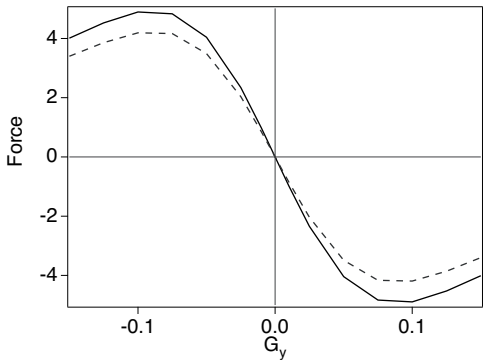

FIGURE 8. Variation of the hydrodynamic force on a fixed cylinder as a function of its position y in the aperture determined from numerical simulations. ♦: total force F_y; ▲: pressure component of F_y; vertical dashed dotted lines: approximative limits of the linear regime. $Re = 20$.

and shows that equation (5.2) is valid up to $y \simeq 2 \times 10^{-2}$ (vertical lines). For larger displacements, the modulus of the force levels off and then decreases.

In the opposite high frequency limit, F_1 is approximately proportional to f^2 (thick solid line in figure 7) while the phase shift ϕ_1 becomes zero. In the linear regime, F_y is therefore proportional to the second derivative of y, i.e. to the transverse acceleration of the cylinder, with :

$$F_y = -m_a \ddot{y}_{ax}. \tag{5.3}$$

The proportionality coefficient m_a in equation (5.3) represents an added mass associated to the kinetic energy of the fluid; m_a is related to F_1 and A by: $F_1 = m_a(2\pi f)^2 A$. Using a regression on the four last high frequency points in Fig. 8 leads to $m_a = 0.68$ or equivalently to an additional density $\rho_a = 2.0$.

The mass and stiffness force terms do not induce any net exchange of energy between the flow and the cylinder: the average over one period of the product of either of these terms by $\dot{y}_{ax}$ (representing the mean power exchanged) is indeed equal to zero. If no other term is present, the phase ϕ_1 can only be equal to 0 or π, which is not in agreement with figure 7: additional dissipative force terms must therefore be introduced. A logical choice is to add a term proportional to the velocity $\dot{y}_{ax}$: we assume therefore the following expression of the global lift force:

$$F_y = -m_a \ddot{y}_{ax} - \alpha_0 \dot{y}_{ax} - ky. \tag{5.4}$$

The coefficient α_0 is determined by equating the expressions of the average energy exchange over one period deduced from equations 5.4 and 5.1. One obtains:

$$\alpha_0 = \frac{F_1}{2\pi f A} \sin(\phi_1), \tag{5.5}$$

in which F_1 and ϕ_1 are given by the simulations of forced oscillations. The sign of α_0 is therefore the same as that of $\sin(\phi_1)$ and characterises the stability of the system: for $\alpha_0 > 0$, the energy of the cylinder increases during one period (unstable case) while, for $\alpha_0 < 0$, it loses energy (stable case). In the phase variation curve in figure 7, one sees that $\sin(\phi_1)$ (and therefore α_0) is negative at high frequencies (above $f \simeq 1.4$) and positive at lower ones.

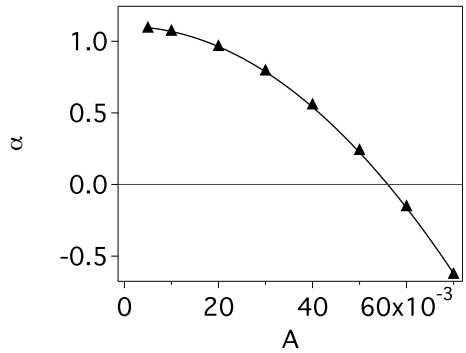

FIGURE 9. Variation of the amplification coefficient α with the amplitude A of a forced oscillation of the cylinder. Oscillation frequency $f = 1.46$; $Re = 20$. ▲: numerical simulation results, solid line: parabolic fit.

5.2. *Force response to a large amplitude excitation*

As the amplitude A is increased, the response of the lift force becomes non-linear and equation 5.4 is no longer valid. In order to analyse its variation with time, the force is decomposed into a Fourier series:

$$F_y(t) = \sum_{q=1}^{\infty} F_q \sin(2\pi q f t + \phi_q), \tag{5.6}$$

in which the phases ϕ_q are chosen so that $F_q \geqslant 0$.

As for the linear regime, the coefficient α generalising α_0 is estimated numerically by computing the average power transferred to the cylinder over one period. Using the decomposition of F_y into a Fourier series leads to: $\alpha = (F_1/2A\pi f)\sin(\phi_1)$. The variation of α with A, determined by numerical simulations for a fixed frequency, is displayed in figure 9; it is well fitted by:

$$\alpha = \alpha_0 - (\beta/4)A^2, \tag{5.7}$$

in which α_0 is the value in the low amplitude regime. The force term $\alpha_0 \dot{y}_{ax}$ of equation 5.4 becomes then, still for sine wave forced oscillations:

$$F_y = (\alpha_0 - \beta y^2)\dot{y}_{ax}. \tag{5.8}$$

At different frequencies, the variation of α with respect to the amplitude A is similar: in all cases, the coefficient characterising the gain of energy decreases with the amplitude up to a critical value above which energy must be input externally to keep A constant.

As the amplitude A increases, the stiffness k also varies. Figure 8 shows that, outside the linear domain sketched by the two vertical dotted lines, the effective stiffness k decreases with A. However, this variation is small enough to change quantitatively but not qualitatively the dynamics of the cylinder. It is shown in the following sections that the characteristics of the oscillation are well approximated by assuming a constant stiffness k.

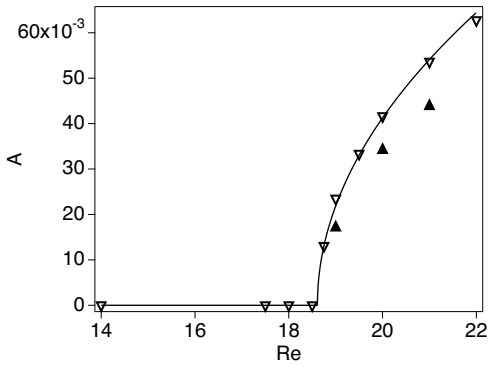

FIGURE 10. Amplitude of the free oscillations in the stationary regime as a function of Re for $\rho_s = 0.01$. ∇: numerical simulation results for free oscillations; $\blacktriangle$: predictions from the Van der Pol equation (6.5); solid line: fit by a square root variation.

6. Free oscillations.

6.1. *Equation of motion of a free cylinder and Van der Pol oscillator.*

For a free cylinder, the global hydrodynamic force F_y on the cylinder is related to its acceleration $\ddot{y}_{ax}$ by Newton's second law:

$$m_s \ddot{y}_{ax} = F_y. \tag{6.1}$$

Moreover, the relations (5.4) and (5.8) between F_y and the displacement y and its time derivatives remain valid. Equation 6.1 becomes then:

$$(m_a + m_s)\ddot{y}_{ax} - (\alpha_0 - \beta(y)^2)\dot{y}_{ax} + ky = 0, \tag{6.2}$$

which shows that the position of the cylinder verifies the classical Van der Pol equation (see for example **??**). Close to the threshold, the oscillation is quasi-sinusoidal. The frequency f_l and the growth rate ξ of the oscillations predicted by equation (6.2) are then related to its parameters by:

$$f_l = \frac{1}{2\pi}\sqrt{\frac{k}{m_a + m_s}}, \tag{6.3}$$

and:

$$\xi = \frac{\alpha_0}{2(m_a + m_s)}. \tag{6.4}$$

Note that, due to the influence of the mass m_s of the cylinder, the frequency f_l of the free oscillations is lower than the resonance frequency $f_r = \sqrt{k/m}/(2\pi)$ for forced oscillations and decreases with m_s.

The frequency f_l and the growth rate ξ can then be predicted by using in (6.3) and (6.4) the values of k, m_a and α_0 deduced in section 5 from the simulations of forced oscillations. These values are compared in figure 6(a,b) to those obtained from direct simulations of free oscillations in transient regimes (see figures 5c-d). The two sets of values are in good agreement without requiring any adjustable parameter; this confirms the validity of the above description.

In the Van der Pol equation, the sign of α_0 determines whether the system tends towards a fixed point or a limit cycle in the permanent regime: if $\alpha_0 < 0$, the cylinder remains motionless half way between the walls, and if $\alpha_0 > 0$, it oscillates spontaneously. In this latter case, the amplitude A of the oscillation is then limited by the non-linear

term $-\beta(y)^2\dot{y}_{ax}$ of (6.2). In the quasi-sinusoidal stationary regime, A is given by:

$$A = 2\sqrt{\alpha_0/\beta}. \tag{6.5}$$

Like f_l and ξ, the amplitude may therefore be computed by using in equation (6.5) values of α_0 and β obtained from numerical simulations of forced oscillations. In the same range of Reynolds numbers as above, these values have a similar variation as those corresponding to free oscillations (figure 10). Above the threshold, the variation of A is well-fitted by a variation proportional to $\sqrt{Re - Re_c}$.

Overall, the free oscillations of the cylinders display several clear-cut features: weak variation of the frequency near Re_c, continuous increase of ξ from negative values below Re_c to positive ones above and amplitude increasing as $\sqrt{Re - Re_c}$. These features are all characteristic of a supercritical Hopf bifurcation, which is the usual bifurcation for a system described by a Van der Pol equation.

The expressions of the frequency, growth rate and amplitude given above are only valid in the quasi-sinusoidal regime. It is possible to verify that the oscillations are quasi-sinusoidal directly from the Van der Pol equation, by computing the quality factor $Q = 2\pi f_r m_a/\alpha_0$. Near the threshold, the quality factor is very high ($Q = 23$ at $Re = 20$) as expected and the oscillation is quasi-sinusoidal at the frequency f_l both in the transient and permanent regime. For Re farther from the threshold, the quality factor decreases ($Q = 2.4$ at $Re = 30$) but remains large enough to obtain quasi-sinusoidal oscillations.

It must finally be pointed out that the Van der Pol equation involves directly the transverse displacement y from equilibrium and its first and second time derivatives instead of a typical velocity of a wake like in the study of vortex-induced vibrations by **?**.

6.2. *Influence of the mass of the cylinder on the stability of the free oscillation.*

As mentioned above, a free cylinder oscillates spontaneously at the frequency $f_l = 1/2\pi\sqrt{k/(m_a + m_s)}$ only if $\alpha_0 > 0$ (or equivalently $\sin(\phi_1) > 0$). The range of values of Re for which this condition is satisfied and its dependence on m_s may be inferred from figure 11 representing $\sin(\phi_1)$ as a function of frequency at different Reynolds numbers.

For $Re = 14$ (case a), $\sin(\phi_1)$ is always negative even if the frequency f_l is shifted toward lower values by increasing the mass m_s: the cylinder remains therefore at rest regardless of m_s.

For $Re = 16.5$ (case b), one has still $\sin(\phi_1) < 0$ at f_r thus a massless cylinder does not oscillate. However, when f_l is reduced by increasing m_s, $\sin(\phi_1)$ becomes positive and the oscillations appear. This means that the increased inertia of denser cylinders reduces the threshold Reynolds number Re_c.

Increasing again Re to 20 (figure 7) or 30 (figure 11c), $\sin(\phi_1)$ is positive at all frequencies lower than f_r: the cylinder oscillates regardless of its density.

For $Re = 50$ (case d), $\sin(\phi_1)$ is positive for $f = f_r$ and negative at low frequencies. In contrast with case b, dense cylinders remain stable while the massless one oscillates.

The effect of the mass on the oscillation is also illustrated in Fig 12 which shows the variations of the amplitude and frequency as function of the Reynolds number. As mentioned in the previous paragraph, cylinders with a density above 4 (triangles, crosses and diamonds in Fig 12) stop to oscillate when the flow velocity is increased. This regime ends when the Reynolds number meets the critical Re above which vortex shedding appears (110 for this geometry). The cylinder then oscillates anew but with a much lower amplitude ($A \sim 0.1$). In the same time, the frequencies lock in with the natural frequency of the system and the reduced frequency f becomes constant and close to 1.
The extent of the regime over which an extinction of the oscillation is observed increases

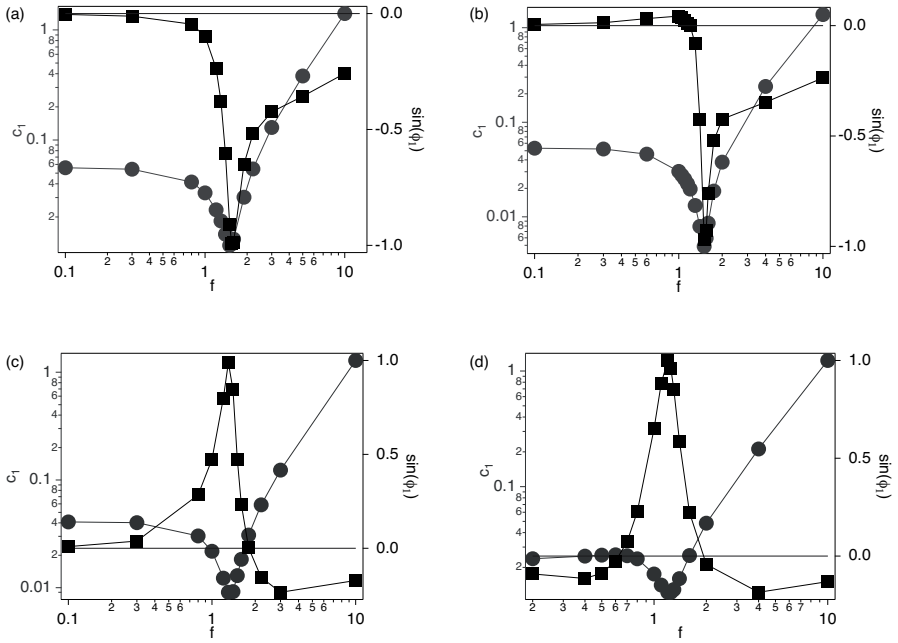

FIGURE 11. Variation of the amplitude F_1 (•) and the sine of the phase ϕ_1 (■) of the hydrodynamic force as a function of the forced oscillation frequency f at different Reynolds numbers Re. Amplitude $A = 5 \times 10^{-4}$. (a): $Re = 14$, (b): $Re = 16.5$, (c): $Re = 30$, (d): $Re = 50$.

FIGURE 12. Influence of the mass of the cylinder on the variation of the amplitude and the frequency of the free oscillations as a function of Re (from numerical simulations). (a): amplitude, (b): frequency (only defined if the amplitude is not vanishing). □: $\rho_s = 0.01$; ○: $\rho_s = 1.19$; ×: $\rho_s = 4$; ◇: $\rho_s = 5$, +: $\rho_s = 7$, △: $\rho_s = 15$. Dashed horizontal line: maximum possible amplitude. •: frequency of the instability flow downstream a fixe cylinder.

with the cylinder mass. Below a critical density, the oscillations are not found to stop; a continuous increase of A and decrease of f are observed. In these cases, the oscillations are not found to lock in with the natural frequency.

The different behavior of the cylinder with the flow conditions and its mass are displayed in Fig.13. The extinction domain separating the confined (filled circles) and vortex (crosses) induced vibration regimes (empty circles in Fig.13) clearly highlight the existence of a critical mass below which both regimes coexist (for ρ_s between 4 and 6) or only the CIV regime.

The variations of the amplitude and the frequency are displayed in figure 12, for both the low Re (< 50) on which this article focuses and higher Re up to above the instability downstream a fixe cylinder. At low Re, this figure illustrates the results of the forced oscillations discussed in this §: the threshold Reynolds number decreases from 19 to 15 as the density ρ_s varies from 0 to 15, and the frequency decreases when the density increases (see (6.3)). For Re between 20 and 30, the amplitude follows the same trend for all densities. For the densest cylinder ($\rho_s = 15$), the amplitude reaches a maximum for $Re \simeq 30$ and the cylinder is again stable for $Re \geqslant 50$. The disappearance of the oscillations also occurs for $\rho_s = 5$ and $\rho_s = 7$ at a Re which decreases when the density increases. At a Re close (but lower than) the threshold of the oscillation of the flow

FIGURE 13. Phase diagram of the behaviour of the cylinder for different Re and ρ_s, obtained numerically. ○: cylinder stable in the midplane of the walls, ●: confined regime oscillations, +: oscillations induced by vortex emission. The grey regions are guide for the eye.

downstream a fixe cylinder, these cylinders oscillate again, at a very low amplitude and, importantly, at a frequency very close to the one of the flow instability. This is in contrast with the behaviour of the cylinders of low density ($\rho_s = 0.01$ and $Re = 1.19$) which oscillate for all frequencies above the (first) threshold Re_c, and which seems to be unaffected by the flow instability. The difference of the behaviour at low (< 50) and high Re confirms that the instability on which we focus in this article is not linked to a flow instability downstream a fixe cylinder.

The figure 12 allows us to define three different behaviours of the cylinder. The cylinder may remain stable in the midplane of the walls, or may oscillate. Two regimes of oscillations are observed: a first one, called here 'confined regime oscillations', has a frequency which depends on the density in agreement with (6.3), and a second one, called here 'vortex shedding induced oscillations', where the frequency is almost constant for all density and linked directly to the flow downstream a fixe cylinder. The behaviour of the cylinder as a function of Re and ρ_s is displayed in figure 13. The cylinder is stable at very low ($<\sim 15$) Re and at intermediate Re for high densities. The confined regime oscillations is observed at low Re (between ~ 17 and ~ 40) for all densities, and at all the reported Re for low densities (< 3). At high densities and Re, the cylinder oscillates due to the instability (or the low stability) of the flow downstream a fixe cylinder. Figure 13 is a first attempt to determine the behaviour at high Re ; the transitions to the restabilisation and to the vortex shedding emission will be addressed in a future study.

7. Hydrodynamic interpretation of the coefficients of the Van der Pol equation.

The equation (6.2) accounts well for the growth (or decay) of the oscillations with time and for the relation between measurements on forced and free oscillations. However, this global dynamical system approach does not provide information on the physics of the flow at the local scale. In this part, we investigate the relation between the coefficients of the equation and the characteristics of the flow field.

7.1. *Origin of the stiffness coefficient*

The stiffness coefficient - defined by equation (5.2)- characterizes the restoring force exerts on a fixed cylinder away from the center of the Hele Shaw cell. As seen in figure 8, the total force F_y is mainly due the pressure component: its value can be interpreted from the pressure field displayed in figure 14(b,d) for $Re = 1$ and 20. The pressure variation is particularly important in the region separating the cylinder and the walls, referred to as *channels* in the following.

For $Re = 1$, there is a fore-aft symmetry of both the velocity and the pressure gradient (see figure 14a,b) because the viscous effects are dominant. Due to this symmetry, the lift force F_y vanishes (almost), regardless to the position of the cylinder in the gap. This is no longer the case for $Re = 20$ (see figure 14c,d). In that case, the pressure on the surface of the cylinder is higher in the upper (narrower) channel than in the lower (larger) channel, for all values of x (between $-D/2$ and $D/2$). As a result, the global resultant

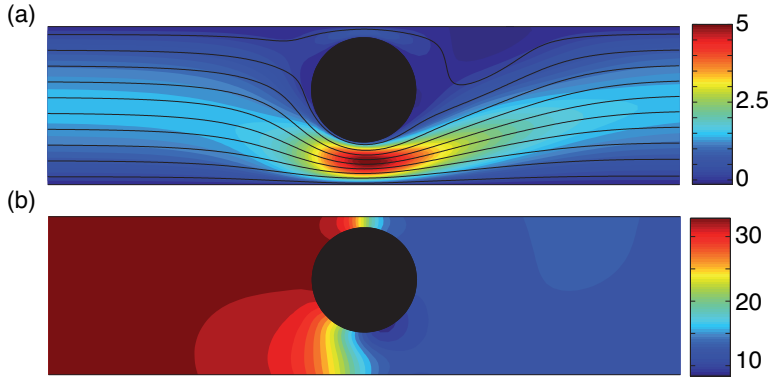

FIGURE 14. Numerical simulation of the flow (from left to right) around a fixed cylinder at $Re = 1$ and $Re = 20$. (a) Colour bar (resp. grey levels) velocity component v_x at $Re = 1$; continuous lines: streamlines. (b) Colour bar (resp. grey levels) pressure field at $Re = 1$. (c) Colour bar (resp. grey levels) velocity component v_x at $Re = 20$; continuous lines: streamlines. (d) Colour bar (resp. grey levels) pressure field at $Re = 20$.

force is non zero and oriented downwards: it acts as a restoring force, in agreement with figure 8.

Because the pressure is almost uniform upstream and downstream the cylinder, the higher pressure at a given x in the upper (narrower) channel can be explained by the fact that the pressure gradient is more symmetrical about the axis $x = 0$ in this later channel. The asymmetry along y in a channel is indeed due to inertial effects, and is more pronounced when Re increases. The local Re is significantly higher in the lower (larger) channel than in the upper (narrower) one due to larger local width and velocity, which explains the observed pressure field at $Re = 20$.

At lower values of the dimensionless diameter D, the result might have been different as shown by **?** for $D = 0.2$. In this case, a contribution to the force due to the curvature of the velocity profile leads to two symmetrical additional equilibrium positions which are not in the mid-plane between the walls.

7.2. *Added mass*

Forces proportional to the acceleration of a solid body in a fluid are classical in fluid dynamics. Such forces are partly due to the acceleration of the fluid, and are thus observed even in irrotational flows. For an irrotational fluid without base flow, the additional density can be estimated numerically, and is equal to $\rho_a = 1.44$ at $y = 0$. This is lower than the values $\rho_a = 3$ calculated from the stiffness and the resonance frequency. It also differs from the value $\rho_a = 2$ deduced from the forced oscillations at $f = 10$ (using $m_a = F_1/(A(2\pi f)^2)$). These differences may be due to the relatively low value of Re or

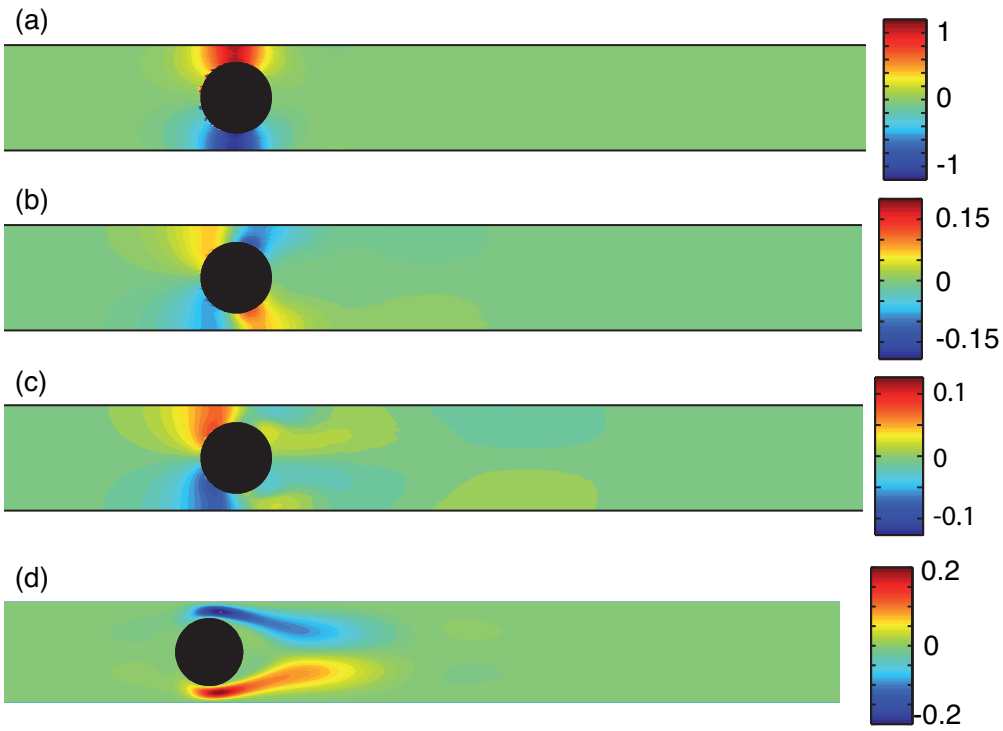

FIGURE 15. (Colour online) Maps of the pressure perturbation $\delta p(x, y)$ induced by an upwards motion of the cylinder at a velocity $\dot{y}_{ax} = 0.013$, as a function of Re (from numerical simulations of forced oscillations at $f = 0.2$). (a) $Re = 1$, (b): $Re = 20$, (c): $Re = 50$, (d): Bernoulli's pressure difference term for $Re = 20$.

to the influence of the base flow. Other authors have also reported values of the added mass differing from the potential case for vortex-induced vibrations (see **?**).

7.3. *Destabilising force term.*

Here, we analyse the origin of the term $\alpha_0 \dot{y}_{ax}$ by considering the variations of pressure $\delta p(x, y) = p(x, y) - p_0(x, y)$ between the case of a forced oscillation ($p(x, y)$) and that of a static cylinder $p_0(x, y)$. The frequency $f = 0.2$ is low enough so that the influence of the added mass is negligible; the pressure field corresponds to a transverse location $y = 0$ of the cylinder at which the stiffness term ky becomes zero. Figures 15a-c display the pressure perturbations corresponding to three different Reynolds numbers (the force F_y on a fixed cylinder at $y = 0$ vanishes due to the symmetry, and the use of the perturbation of the pressure δp instead of the pressure p is justified by the clarity of the figure).

At the lowest Reynolds number $Re = 1$ (case a), δp is positive above the cylinder and negative below it (see figure 15a): the orientation of the resultant force is therefore opposite to the cylinder velocity so that α_0 is negative and the system is stable. In this case, due to the linearity of Stokes equation, the force is equal to the Stokes drag on a cylinder moving in a fluid at rest, which always opposes the motion.

For $Re = 20$ (case b), two additional lobes appear downstream the cylinder: their signs are opposite to that of the previous ones and the magnitude of the corresponding pressure variation is larger: the resultant force is then in the same direction as the

cylinder velocity. In this case, α_0 is positive (for $f = 0.2$) and the oscillation is amplified (at least if $f_l = f$).

For $Re = 50$ (case c), the downstream lobes disappear while the upstream ones are still present. The pressure is therefore again higher above the cylinder than below, leading to a resultant force in the direction opposite to the cylinder velocity. As a result, $\alpha_0 < 0$ (for $f = 0.2$) and the cylinder is again stable if $f_l = f$, which corresponds to a cylinder of a large mass. The reduction of the downstream lobes may be due to the recirculation zone present behind the cylinder in the base flow.

These results show that the pressure distribution strongly depend on the Reynolds number and, therefore, on the influence of inertia. As a first approach, we tried to estimate its effect by the Bernoulli pressure theorem leading to: $\delta p_B \simeq -\boldsymbol{V}_b.\boldsymbol{v}$ in which $\boldsymbol{V}_b$ and $\boldsymbol{v}$ are the velocities for the base and the perturbated flows respectively (this is only a rough approximation because of the influence of viscous forces, in contrast with the assumptions of the theorem). Low and high pressure regions of the same sign as in the downstream lobes for $Re = 20$ appear indeed. However, no upstream lobes are observed and, moreover, this effect should be stronger for $Re = 50$ instead of disappearing. More refined models taking into account viscous forces are therefore needed.

It is worth noticing that the interpretation of the destabilising term, like that of the effective stiffness and the added mass, does not involve vortex shedding.

8. Conclusion

This paper reports an experimental and numerical study demonstrating the existence of a novel hydrodynamic instability observed when a tethered cylinder is placed in narrow gap. This instability appears above a critical Reynolds number Re_c of the order of 20: this threshold far below the critical Reynolds number above which vortex induced vibration is observed. Close to the instability threshold, the position of the cylinder y verifies a Van der Pol equation, with a linear dissipative term that changes of sign at the threshold. The lack of hysteresis, the square root variation of the amplitude and the continuous increase of the growth rate with Re demonstrate the Hopf like nature of the bifurcation.

The motion of the cylinder is described by three parameters: a stiffness, a mass and a destabilizing terms. The stiffness term has a purely hydrodynamic origin and results from the confinement of the flow. The mass term includes the mass of the cylinder (which may be zero without suppressing the oscillations) and the hydrodynamic added mass. The oscillatory regime is determined by the sign of the third term which is proportional to the velocity.

At low Reynolds numbers, one has only a dissipative viscous drag force leading to damping. At higher Re values, the term changes sign and oscillations may appear: this results from inertial effects but simple explanations in terms of a Bernoulli pressure do not provide a satisfactory picture. Contrary to vortex shedding, the destabilizing force results from subtle tiny variations of the local pressure distribution in the region between the cylinder and the walls. These variations reflect a subtle balance between inertial and viscous effects which depends on the Reynolds number.

For dense cylinder, the confined induced regime ends abruptly and, if the Reynolds increases, new oscillations are observed as soon as the BVK vortex shedding appears. Below a critical mass, oscillations are not observed to stop: future work will study the effect of the vortex shedding on this regime.

As mentioned above, the present work deals with a confined cylinder at low Reynolds number. Further studies should attempt to relate these effects to other works using less confined geometries and/or involving vortex shedding. This may be achieved by

increasing the Reynolds number beyond the onset of the Bénard–Von Kármán instability and to reduce the confinement by decreasing the diameter of the cylinder.

We thank R. Pidoux, C. Borget and A. Aubertin for realizing and developing the experimental set up. We acknowledge A. Lefebvre-Lepot, V. Scelles, B. Maury and S. Faure for their help in the numerical simulations. B. S. was supported by a scholarship from the French Ministry of Research. This work has been greatly facilitated by the RTRA Triangle de la Physique.